Beating Stellar Systematic Error Floors Using Transit-based Densities

Jason D. Eastman[1] , Hannah Diamond-Lowe[2] , and Jamie Tayar[3]

[1] Center for Astrophysics | Harvard & Smithsonian, 60 Garden St., Cambridge, MA 02138, USA; jason.eastman@cfa.harvard.edu
[2] National Space Institute, Technical University of Denmark, Elektrovej 328, 2800 Kgs. Lyngby, Denmark
[3] Department of Astronomy, University of Florida, Bryant Space Science Center, Stadium Road, Gainesville, FL 32611, USA

Abstract

It has long been understood that the light curve of a transiting planet constrains the density of its host star. That fact is routinely used to improve measurements of the stellar surface gravity and has been argued to be an independent check on the stellar mass. Here we show how the stellar density can also dramatically improve the precision of the radius and effective temperature of the star. This additional constraint is especially significant when we properly account for the 4.2% radius and 2.0% temperature systematic errors inherited from photometric zero-points, model atmospheres, interferometric calibration, and extinction. In the typical case, we can constrain stellar radii to 3% and temperatures to 1.75% with our evolutionary-model-based technique. In the best real-world cases, we can infer radii to 1.6% and temperatures to 1.1%—well below the systematic measurement floors—which can improve the precision in the planetary parameters by a factor of two. We explain in detail the mechanism that makes it possible and show a demonstration of the technique for a near-ideal system, WASP-4. We also show that both the statistical and systematic uncertainties in the parallax from Gaia DR3 are often a significant component of the uncertainty in L_* and must be treated carefully. Taking advantage of our technique requires simultaneous models of the stellar evolution, bolometric flux (e.g., a stellar spectral energy distribution), and the planetary transit, while accounting for the systematic errors in each, as is done in EXOFASTv2.

Unified Astronomy Thesaurus concepts: Exoplanet astronomy (486); Planet hosting stars (1242); Stellar evolutionary models (2046); Spectral energy distribution (2129); Measurement error model (1946); Exoplanet detection methods (489); Transit photometry (1709)

1. Introduction

Any measurement of the mass, radius, or temperature of an exoplanet depends directly on those same quantities for its host star. As a result, the exploding interest in exoplanets has rekindled a broad interest in measuring precise and accurate stellar parameters in order to derive precise and accurate planetary parameters. This has correctly given rise to the oft-repeated phrase "know thy star, know thy planet."

Precise parallax measurements and all-sky, precise optical photometry by Gaia (Gaia Collaboration et al. 2016, 2018), coupled with all-sky infrared photometry from the Two Micron All Sky Survey (2MASS; Skrutskie et al. 2006) and the Wide-field Infrared Survey Explorer (WISE; Wright et al. 2010), have enabled a new era of precision stellar astrophysics. Now, for nearly all exoplanet host stars, the uncertainties in stellar parameters are no longer limited by the measurements, but by the stellar evolutionary and atmospheric models, as well as their calibrations, requiring an understanding of the underlying systematic errors in those models and methods. We need great care not to be overly confident in our results, but we must also not be overly conservative, lest we fail to recognize the significance of a precise detection.

Tayar et al. (2022) published a guide for reasonable systematic error floors by carefully enumerating the sources of systematic error, tracing fundamental calibrations back to their origins, and determining the discrepancies between different groups with different instruments and different models. They find systematic errors that are larger than uncertainties often quoted in the exoplanet community.

However, Tayar et al. (2022) do not consider the impact of an additional constraint for transiting exoplanet hosts: the stellar density, ρ_*, measured from the transit light curve. The ability of the transit light curve to measure ρ_* was first recognized by Seager & Mallén-Ornelas (2003) for planets in circular orbits. Planets in eccentric orbits complicate the computation and generally add additional uncertainty, but with a known eccentricity and argument of periastron (typically from radial velocities (RVs), but also potentially through primary and secondary transits or, in the future, astrometry), we can still derive the stellar density from a transit light curve (see, e.g., Eastman et al. 2019).

By definition, we need only two of the parameters stellar mass (M_*), radius (R_*), density (ρ_*), or surface gravity ($\log g_*$) to derive the others, as these are mathematically and exactly related to one another. Then, we only need either the bolometric flux ($F_{\rm bol}$) or stellar temperature ($T_{\rm eff}$)—and a precise distance from Gaia—to determine the other, again, by definition.

This concept is not new. Sandford & Kipping (2017) measured precise stellar densities of 66 Kepler planet hosts to help characterize the star. Beatty et al. (2017) argued, and Stevens et al. (2018) later expanded on the idea, that, with an R_* from spectral energy distribution (SED) fitting and ρ_* from transits, we can derive an M_* free from the systematic errors of stellar evolutionary models. Unfortunately, Stevens et al. (2018) showed—and we will confirm—that even an optimistic statistical uncertainty in the stellar mass we can obtain this way is well above the $\sim$5% that is thought to be a realistic systematic uncertainty in M_* from stellar models. In addition,

they still must rely on systematics-dominated determinations of $F_{\rm bol}$ to infer the stellar radius in the first place.

Here we show an idea similar to that found in Stevens et al. (2018), but instead of using ρ_* and deriving M_* with a known R_* without an evolutionary model, we use the evolutionary model to derive a more precise R_* from ρ_*. Then, with a measured L_*, we derive a more precise $T_{\rm eff}$. Assuming the systematic error floors from Tayar et al. (2022) on M_* and L_* and the transit-derived measurement of ρ_*, we simply propagate those floors to significantly more precise inferred values of R_* and $T_{\rm eff}$ than the measurement floors found by Tayar et al. (2022) using models alone. We go through the math in Section 2 and discuss systematic errors in Section 3. We talk about best practices in Section 4. Finally, we look at a best-case scenario in refitting WASP-4b in Section 5, and we discuss the implications of this work in Section 6.

2. Mathematical Validation

Throughout this paper, we explain the logic of how the constraints apply by discussing the path through the primary constraints serially. Then, when we propagate the errors, we assume that we have independent measurements of each quantity at each step. In reality, the constraints are not independent, and such a serial derivation would erroneously count each measurement multiple times. We must fit all models with all constraints simultaneously within a global model to avoid this. However, the error propagation within such a global model is complex and makes it difficult to develop an understanding of where the information comes from. The excellent agreement between the errors we derive with our simplified, analytic approach and the global, simultaneous model performed by EXOFASTv2 implies that the correlations between constraints are minimal and validates our simplification as a useful pedagogical tool to develop this critical intuition. For details about how EXOFASTv2 implements these model systematic floors within our simultaneous global model, we refer the reader to the stellar model section of Eastman et al. (2019).

2.1. M_* from R_*

First, we rederive results similar to those of Stevens et al. (2018), which uses R_* from an SED analysis and ρ_* from a transit light curve to determine M_*. We start with the definition of the stellar density,

$$\rho_* \equiv \frac{3M_*}{4\pi R_*^3}. \tag{1}$$

Assuming Gaussian and uncorrelated errors, we can use standard error propagation techniques to show that the uncertainty in M_*, σ_{M_*}, is given by

$$\sigma_{M_*}^2 = \left(\frac{\partial M_*}{\partial \rho_*}\right)^2 \sigma_{\rho_*}^2 + \left(\frac{\partial M_*}{\partial R_*}\right)^2 \sigma_{R_*}^2, \tag{2}$$

where σ_{ρ_*} is the uncertainty in the stellar density measured from transits and σ_{R_*} is the uncertainty in the stellar radius derived from $F_{\rm bol}$.

To evaluate Equation (2), we solve Equation (1) for M_*,
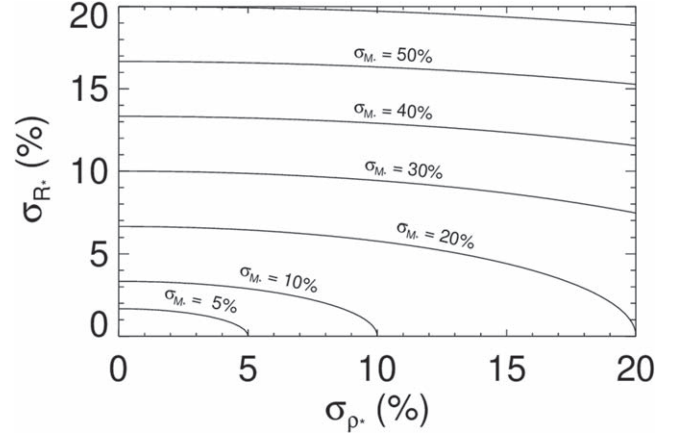
$$M_* = \frac{4\pi R_*^3 \rho_*}{3}, \tag{3}$$

Figure 1. A contour plot of the percent error in M_* as a function of the percent errors in ρ_* and R_*, derived from Equation (7). We see that the dependence on σ_{R_*} is strong, and with a typical σ_{ρ_*} of 10%, the resulting constraint on M_* is not particularly informative. Even with no error in ρ_*, the systematic floor in R_* of ∼4.2% implies an error of 13% in stellar mass, which is much larger than the ∼5% presumed for masses derived from evolutionary models.

evaluate each derivative,

$$\frac{\partial M_*}{\partial \rho_*} = \frac{4\pi R_*^3}{3}, \tag{4}$$

$$\frac{\partial M_*}{\partial R_*} = 4\pi R_*^2 \rho_*, \tag{5}$$

and plug into Equation (2)

$$\sigma_{M_*}^2 = \left(\frac{4\pi R_*^3 \sigma_{\rho_*}}{3}\right)^2 + (4\pi R_*^2 \rho_* \sigma_{R_*})^2. \tag{6}$$

This equation simplifies dramatically and makes the error dependence more intuitive if we divide both sides by M_*^2 (Equation (3)) to express the uncertainties as fractions:

$$\left(\frac{\sigma_{M_*}}{M_*}\right)^2 = \left(\frac{\sigma_{\rho_*}}{\rho_*}\right)^2 + \left(\frac{3\sigma_{R_*}}{R_*}\right)^2. \tag{7}$$

In Figure 1, we show a contour plot of the percent error in M_* as a function of the percent errors in ρ_* and R_*, using Equation (7). We see that the percent error in R_* is multiplied by a factor of three as it propagates to the error in M_*, which makes it difficult to get a small σ_{M_*} from R_* and ρ_*.

Stevens et al. (2018) do three simulated fits, one with $e = 0$ (fixed), $b = 0$; one with $e = 0.5$, $b = 0$; and one with $e = 0$ (fixed), $b = 0.75$, to show the dependence on the measured precision of ρ_* on the eccentricity and impact parameter. The percent errors from their simulations on R_*, M_*, ρ_*, and $T_{\rm eff}$ are summarized in Table 1.

While their quoted uncertainty in R_* ignores the often dominant sources of systematic error, we can still use these results to confirm our expectations given Figure 1 and Equation (7). Indeed, in the first case, with 5.1% errors on ρ_* and 1.6% errors on R_*, Equation (2) predicts a 7.0% uncertainty in M_*, completely consistent with the measured value of 7.3%. In the second case, with 17.1% errors on ρ_* and 1.6% errors on R_*, Equation (2) predicts a 17.8% uncertainty in M_*, completely consistent with the measured value of 18.3%. And finally, in the last case, with 16.1% errors on ρ_* and 1.7%

Table 1
Summary of Relevant Parameters from Simulated Fits by Stevens et al. (2018)

	$e = b = 0$	%	$e = 0.5, b = 0$	%	$e = 0, b = 0.75$	%
M_*	$1.146^{+0.075}_{-0.092}$	7.3%	$1.20^{+0.21}_{-0.23}$	18.3%	$1.18^{+0.23}_{-0.19}$	17.8%
R_*	$1.046^{+0.017}_{-0.016}$	1.6%	$1.043^{+0.017}_{-0.018}$	1.6%	$1.047^{+0.018}_{-0.017}$	1.7%
ρ_*	$1.424^{+0.049}_{-0.097}$	5.1%	$1.49^{+0.23}_{-0.28}$	17.1%	$1.46^{+0.26}_{-0.21}$	16.1%
T_{eff}	5710^{+160}_{-140}	2.6%	5740^{+160}_{-150}	2.7%	5700^{+170}_{-140}	2.7%

Note. Percent errors were calculated by averaging upper and lower errors.

errors on R_*, we predict a 17.0% uncertainty in M_*, again consistent with the measured value of 17.8%.

The uncertainty in M_*, even in the best case they present and ignoring systematic errors in F_{bol} when they derive R_*, is well above the ~5% systematic uncertainties presumed in most stellar models because the stellar radius uncertainty is compounded, leading to a much larger percent error in the stellar mass.

For certain ideal systems (tidally circularized, deep, well measured, like WASP-4), the error on ρ_* can be ~1%. Even so, coupled with the 4.2% systematics-dominated uncertainty in R_* recommended by Tayar et al. (2022), the resultant mass uncertainty is still ~13%. We also note that the uncertainty in T_{eff} from Stevens et al. (2018) is relatively large because they have avoided using an evolutionary model, and so the SED is working to constrain both R_* and T_{eff}.

Hence, while their method may serve as a rough, independent check on systematics, it is unlikely to be helpful in a significant number of cases.

2.2. R_* from M_*

Instead, we can infer R_* from M_* and ρ_*. Again, starting from Equation (1), we instead propagate the uncertainties in M_* to R_*:

$$\sigma^2_{R_*} = \left(\frac{\partial R_*}{\partial \rho_*}\right)^2 \sigma^2_{\rho_*} + \left(\frac{\partial R_*}{\partial M_*}\right)^2 \sigma^2_{M_*}. \quad (8)$$

As before, we evaluate and simplify by dividing both sides by R_*^2 to express it as a percent uncertainty:

$$\left(\frac{\sigma_{R_*}}{R_*}\right)^2 = \left(\frac{\sigma_{\rho_*}}{3\,\rho_*}\right)^2 + \left(\frac{\sigma_{M_*}}{3M_*}\right)^2. \quad (9)$$

Here we see that, instead of magnifying the errors as when we determined M_*, our input fractional errors are reduced by a factor of 3. Thus, the resultant percent uncertainty in R_* can be much lower than the input percent uncertainties in M_* and ρ_*.

Figure 2 shows the same contour plot, but now with the propagated percent error in R_* as a function of percent errors in ρ_* and M_* (Equation (9)). Of course, getting M_* usually requires stellar evolutionary models, but even assuming a systematic floor of 5% on M_* from stellar models, if we measure ρ_* to 1%, we get 1.7% errors on R_*—almost three times better than the recommended systematic floor in the stellar models. And while our determination of the stellar radius hinges on the systematics-dominated stellar evolution models, these errors are already included in the computation as σ_{M_*}. For everything else, we rely on well-established physics (i.e., Kepler's law) and definitions (e.g., Equation (1)), though it is important to understand the potential sources of systematic error in ρ_*, discussed in Section 3.
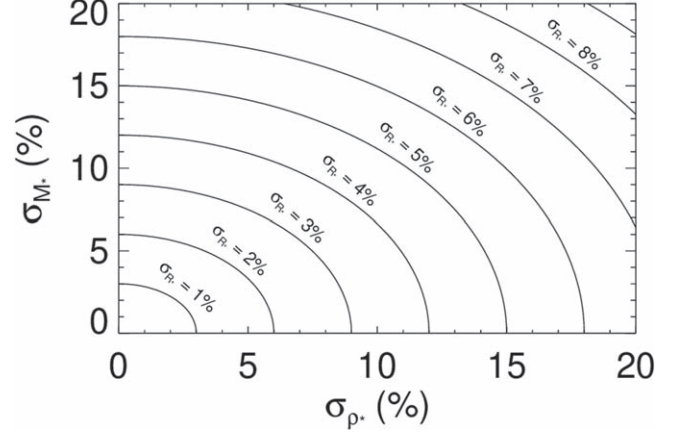

Figure 2. A contour plot of the percent error in R_* as a function of the percent errors in ρ_* and M_*, derived in Equation (9). We see that the dependence on M_* is much weaker, and with a typical σ_{ρ_*} of 10%, the resulting constraint on R_* can be well below the systematic floor from evolutionary models. In the best cases, we can measure ρ_* to ~1%, resulting in R_* uncertainties of ~1.7% —almost entirely dominated by the systematic floor in M_*.

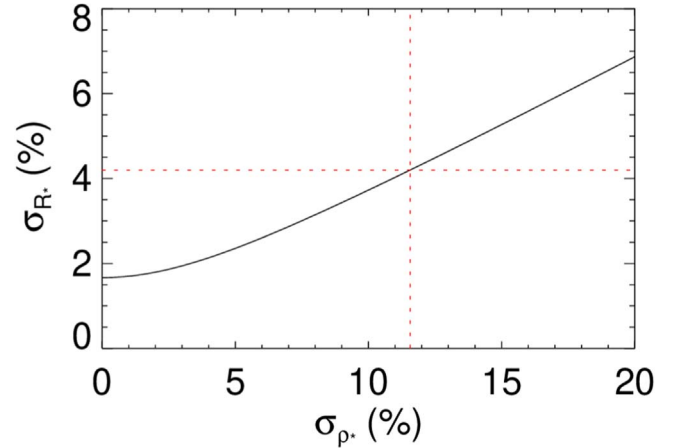**Figure 3.** A plot of σ_{R_*} as a function of σ_{ρ_*}, assuming $\sigma_{M_*} = 5\%$. The break-even point, where $\sigma_{R_*} = 4.2\%$ from Tayar et al. (2022), is shown as a vertical red dashed line and corresponds to $\sigma_{\rho_*} \sim 11.5\%$.

Assuming that our M_* error is 5%, we can plot σ_{R_*} as a function of σ_{ρ_*}, as shown in Figure 3, where the break-even point is shown as a vertical red dashed line at ~11.5%. That is, measuring ρ_* to better than 11.5%—which is typical—allows us to measure the stellar radius to better than the systematic errors identified by Tayar et al. (2022).

2.3. T_{eff} from L_*

Now we can propagate the error in R_* along with a reasonable floor in L_* to T_{eff} with the definition of the stellar
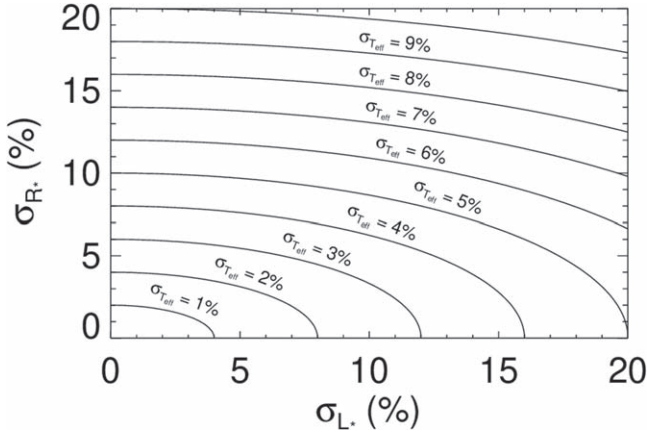
Figure 4. A contour plot of the percent error in T_{eff} as a function of the percent errors in R_* and F_{bol}, derived from Equation (11). We see that the dependence on M_* is much weaker, and with a typical σ_{R_*} of 3% and a systematic floor of $L_* \sim 2.4\%$, the resulting constraint on T_{eff} can be $\sim 1.5\%$—well below the systematic floor from evolutionary models, SED models, or spectra. In the best cases, we can measure R_* to $\sim 1.7\%$ and T_{eff} uncertainties of just under 1%.

luminosity,

$$L_* \equiv 4\pi R_*^2\, \sigma_{SB} T_{eff}^4, \tag{10}$$

where σ_{SB} is the Stefan–Boltzmann constant. Following a similar procedure to that above, we write

$$\sigma_{T_{eff}}^2 = \left(\frac{\partial T_{eff}}{\partial L_*}\right)^2 \sigma_{L_*}^2 + \left(\frac{\partial T_{eff}}{\partial R_*}\right)^2 \sigma_{R_*}^2. \tag{11}$$

Again, we evaluate and simplify by dividing by T_{eff}^2 to express it in terms of fractional errors:

$$\left(\frac{\sigma_{T_{eff}}}{T_{eff}}\right)^2 = \left(\frac{\sigma_{L_*}}{4\,L_*}\right)^2 + \left(\frac{\sigma_{R_*}}{2R_*}\right)^2. \tag{12}$$

We see that the fractional uncertainty in L_* is cut by a factor of 4 as it propagates to T_{eff}, so the uncertainty in R_* quickly dominates. Even so, the uncertainty in R_* is also halved, leading to surprisingly precise determinations of T_{eff}.

Figure 4 shows a contour plot of Equation (12), and we see that, for the recommended systematic error floor of 2.4% on L_* from Tayar et al. (2022) and our best-case error on R_* of 1.7% above, we get 0.9% errors on T_{eff}. That is 50 K for a solar-type star—far better than the typically assumed systematic error floors on T_{eff}, which are derived from the complexities of calibrations and gaps in our knowledge of stellar evolution and atmospheres. Instead, these are very simply derived from an independent constraint on ρ_* (based on Kepler's law) and error propagation, with well-motivated systematic error floors on L_* and M_* from Tayar et al. (2022).

If we assume that $\sigma_{M_*} = 5\%$, we compute the same σ_{R_*} as in Section 2.2. Then, we assume $\sigma_{L_*} = 2.4\%$ and plug those into Equation (12) to plot $\sigma_{T_{eff}}$ as a function of σ_{ρ_*}, in Figure 5. The break-even point is shown as a vertical red dashed line at $\sigma_{\rho_*} \sim 10.3\%$. That is, measuring the precision in ρ_* to better than 10.3% can improve the precision of the T_{eff} to better than the 2% error floor from Tayar et al. (2022).

We note that large systematic errors in L_*—far exceeding the 2.4% suggested by Tayar et al. (2022)—are possible if we fail to identify visual or bound companions that are blended in the broadband photometry. This would introduce large systematic errors in the SED model, increasing the inferred
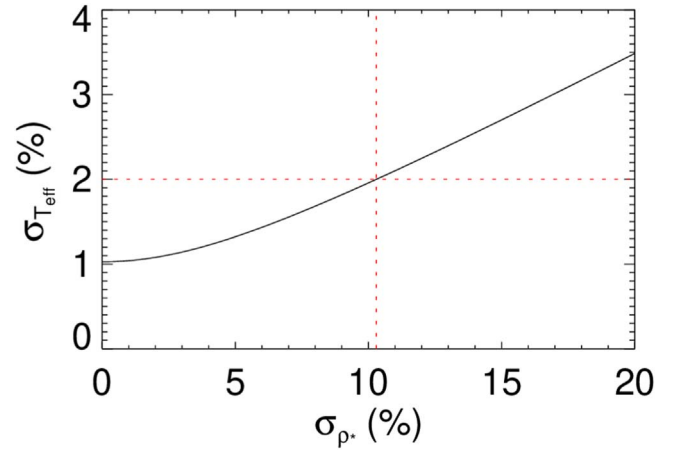

Figure 5. A plot of $\sigma_{T_{eff}}$ as a function of σ_{ρ_*}, assuming $\sigma_{M_*} = 5\%$. The break-even point, where $\sigma_{T_{eff}} = 2.0\%$ from Tayar et al. (2022), is shown as a vertical red dashed line and corresponds to $\sigma_{\rho_*} \sim 10.3\%$.

stellar radius and/or temperature. However, these biases are subject to the same sort of scaling—a bias of 5% in T_{eff} would require an undetected companion with 20% of the flux of the primary, which would likely be detected in high-resolution spectroscopy.

2.3.1. Bolometric Flux, Distance Systematics

We can also write the T_{eff} uncertainty in terms of the bolometric flux, which is the observed quantity,

$$F_{bol} \equiv \sigma_{SB} T_{eff}^4 \left(\frac{R_*}{d}\right)^2, \tag{13}$$

where d is the distance to the star. Following our usual procedure, the fractional uncertainty in T_{eff} becomes

$$\left(\frac{\sigma_{T_{eff}}}{T_{eff}}\right)^2 = \left(\frac{\sigma_d}{2d}\right)^2 + \left(\frac{\sigma_{F_{bol}}}{4F_{bol}}\right)^2 + \left(\frac{\sigma_{R_*}}{2R_*}\right)^2. \tag{14}$$

When the uncertainty in the distance is negligible, Equations (12) and (14) are functionally identical. Tayar et al. (2022) state that the vast majority of planet-hosting stars have negligible distance uncertainties, and they ignore the distance term, not distinguishing between systematics in F_{bol} and systematics in L_*.

Indeed, 75% of planet-hosting stars have fractional distance uncertainties less than the 4.2% systematic stellar radius floor they found, and so the uncertainty in radius usually dominates the error budget in L_* without an external constraint on ρ_* from transits. However, only 40% of planet hosts have distance uncertainties below 1.7%—the smallest systematic uncertainty in the radius we might expect using our method. Therefore, the uncertainty in the parallax—and its systematic uncertainty—is an important consideration in general, even for nearby planet-hosting stars.

We clarify that the systematic floor quoted on L_* from Tayar et al. (2022) is entirely based on the systematic errors inherent in F_{bol}, leaving an important additional source of systematic error in the luminosity from the distance.

There has been a wide recognition that Gaia DR2 has systematic errors in the measured parallax, with estimates ranging from 30 to 80 μas that likely depend on magnitude, color, and ecliptic latitude (Lindegren et al. 2018;
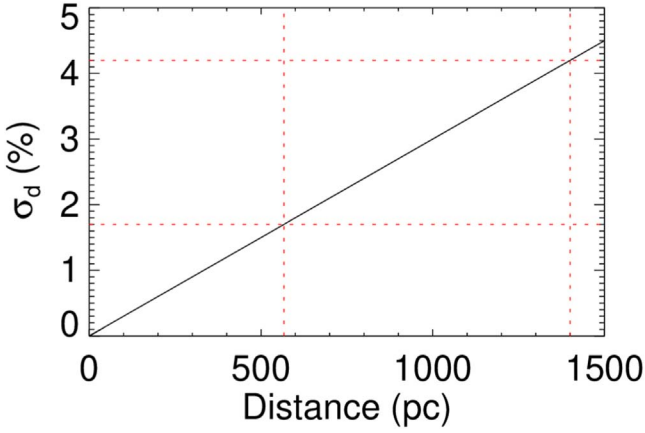
Figure 6. A plot of the level of systematic error in Gaia as a function of distance. The black line shows a 30 μas systematic uncertainty in Gaia DR3 estimated by Lindegren et al. (2021), which dominates the luminosity systematics at $\sim$600 and $\sim$1400 pc when the R_* uncertainties are at the systematic limits of 1.7% and 4.2%, respectively, marked as red dashed lines.

Stassun & Torres 2018; Zinn et al. 2019). Gaia EDR3/DR3 is better but still has systematics estimated at the "few tens of μas" (Lindegren et al. 2021).

Because d is determined from the parallax ϖ,

$$d \equiv \frac{1''}{\varpi} \text{pc}, \qquad (15)$$

we can propagate the uncertainty in ϖ, σ_ϖ, to the fractional uncertainty in distance, σ_d/d, as

$$\frac{\sigma_d}{d} = \frac{\sigma_\varpi}{\varpi}. \qquad (16)$$

We plot Equation (16) as a function of distance in Figure 6, assuming a systematic floor of 30 μas from Gaia DR3. This systematic floor is the dominant source in the L_* computation for stars beyond 1400 pc when we assume the $\sigma_{R_*} = 4.2\%$ from Tayar et al. (2022), corresponding to 8% of planet hosts. When we use our systematic floor of 1.7% using a precise ρ_*, the distance systematic is the dominant source of error in L_* when stars are beyond 567 pc, corresponding to 42% of planet hosts.

Hence, these systematics cannot, in general, be ignored. Because Gaia DR3 has significantly reduced systematic errors, its use is highly recommended over Gaia DR2. DR4 is expected to further reduce systematic uncertainties. It is also important to correct for these systematics as best as possible. We note that EXOFASTv2 includes MKTICSED, which applies the EDR3/DR3 correction to the parallax described in Lindegren et al. (2021), which parameterizes the systematic error as a function of color, magnitude, and ecliptic latitude, but it is unclear what magnitude of systematic error remains.

2.4. log g_* from ρ_* and R_*

Measuring log g_* from spectra is both imprecise and inaccurate, with systematic error floors of $\sim$0.1 dex (Torres et al. 2012).

However, using the same procedure as above, we can propagate errors on ρ_* and R_* to log g_* and achieve a precision more than an order of magnitude better. The fact that the transit can constrain log g_* has long been appreciated (e.g., Winn et al. 2008), but it has never been stated in this kind of formalism.
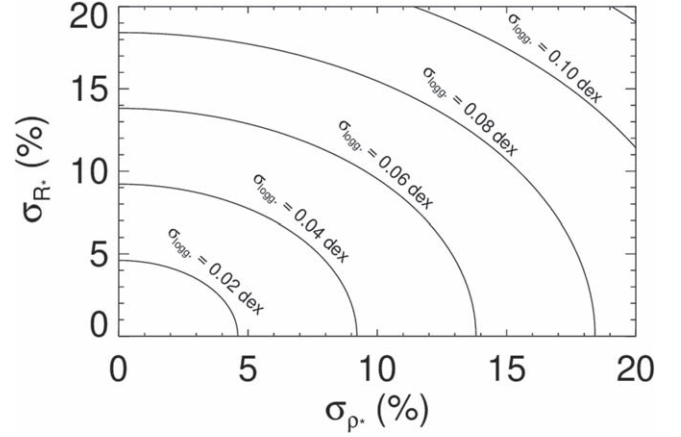

Figure 7. A contour plot of the error in log g_* as a function of the percent errors in ρ_* and R_*, derived from Equation (19). A typical spectroscopic constraint is 0.1 dex. For precise values of ρ_*, we can do more than an order of magnitude better.

We start with the definition of the stellar surface gravity,

$$\log g_* \equiv \log_{10}\left(\frac{GM_*}{R_*^2}\right), \qquad (17)$$

except we refactor to put it in terms of the directly measured ρ_* instead of the systematics-dominated M_*,

$$\log g_* = \log_{10}\left(\frac{4\pi G}{3} \rho_* R_*\right), \qquad (18)$$

and we propagate errors as before,

$$\sigma_{\log g_*}^2 = \left(\frac{\partial \log g_*}{\partial \rho_*}\right)^2 \sigma_{\rho_*}^2 + \left(\frac{\partial \log g_*}{\partial R_*}\right)^2 \sigma_{R_*}^2. \qquad (19)$$

Here the logs already express the log g_* error in terms of the fractional errors in ρ_* and R_*, so we just evaluate the derivatives and simplify:

$$\sigma_{\log g_*}^2 = \left(\frac{\sigma_{\rho_*}}{\ln(10)\,\rho_*}\right)^2 + \left(\frac{\sigma_{R_*}}{\ln(10)R_*}\right)^2. \qquad (20)$$

We show the contour plot of Equation (20) in Figure 7, noting that the error in log g_* is in dex, not percent as for previous, similar plots. A typical spectroscopic constraint on log g_* is 0.1 dex, which is more than an order of magnitude worse for the best cases where $\sigma_{\rho_*} \sim 1\%$ and $\sigma_{R_*} \sim 1.7\%$, where we get an uncertainty of $\sim$0.008 dex.

2.5. log g_* from M_* and R_*

In addition, even propagating sensible systematic error floors in M_* and R_* from evolutionary and SED models, we can typically determine a log g_* that is still more than twice as precise as spectra. That is, in the post-Gaia era, we should only rely on a spectroscopic determination of log g_* in the rare cases where Gaia has not measured the distance of a planet host or when the SED cannot be trusted (e.g., due to a blend).

To show this, we repeat the exercise starting from Equation (17) and again propagate errors,

$$\sigma_{\log g_*}^2 = \left(\frac{\partial \log g_*}{\partial M_*}\right)^2 \sigma_{M_*}^2 + \left(\frac{\partial \log g_*}{\partial R_*}\right)^2 \sigma_{R_*}^2, \qquad (21)$$
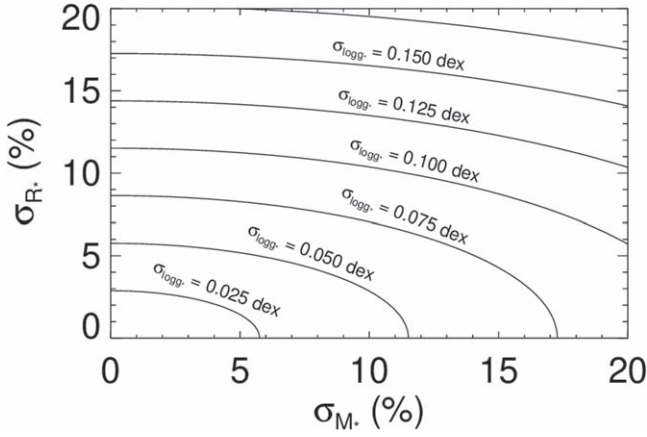
Figure 8. A contour plot of the error in $\log g_*$ as a function of the percent errors in M_* and R_*, derived from Equation (22). A typical spectroscopic constraint of 0.1 dex corresponds to 2% error for a solar-type star. When we get systematic-error-dominated values for M_* and R_* (without a transit density), we still do about $2\times$ better than spectroscopy.

which evaluates to

$$\sigma_{\log g_*}^2 = \left(\frac{\sigma_{M_*}}{\ln(10)M_*}\right)^2 + \left(\frac{2\sigma_{R_*}}{\ln(10)R_*}\right)^2. \quad (22)$$

We show the contour plot of Equation (22) in Figure 8. We can see that for the typical exoplanet host star, which is systematics dominated ($\sigma_{M_*} \sim 5\%$ and $\sigma_{R_*} \sim 4.2\%$), we get a $\log g_*$ precision of ~ 0.042 dex—more than a factor of two better than spectroscopy.

If we assume that our $\sigma_{M_*} = 5\%$, we compute the same σ_{R_*} as in Section 2.2. Then, we plug those into Equation (20) to plot $\sigma_{\log g_*}$ as a function of σ_{ρ_*}, in Figure 9. The break-even point is shown as a vertical red dashed line at $\sigma_{\rho_*} \sim 9\%$. That is, measuring ρ_* to better than 9% can improve the precision of the $\log g_*$ to better than the 0.042 dex derived from the floors in Tayar et al. (2022).

2.6. M_* from $\log g_*$ and R_*

Another proposed avenue to get empirical masses for the star when the host does not have a transiting planet is to derive M_* from a $\log g_*$ obtained from something like Flicker (Bastien et al. 2013, 2016) or asteroseismology plus R_* from an SED. If we propagate the fractional errors in g_* and R_* to M_*,

$$\left(\frac{\sigma_{M_*}}{M_*}\right)^2 = \left(\frac{2\sigma_{R_*}}{R_*}\right)^2 + \left(\frac{\sigma_{g_*}}{g_*}\right)^2, \quad (23)$$

we see that this scaling is more favorable than when starting from ρ_*, but it still requires a precise g_* to be competitive with systematic floors when using stellar models, and the fractional uncertainty in R_* is still doubled as it propagates to M_*.

We note that deriving M_* from a spectroscopic $\log g_*$, while possible, is unlikely to be a competitive approach since the systematic uncertainty in a spectroscopic $\log g_*$ is 0.1 dex (Torres et al. 2012).

3. Systematic Errors in ρ_*

Statistical errors often dominate, and when they do, they are effortlessly propagated throughout the global model. However,
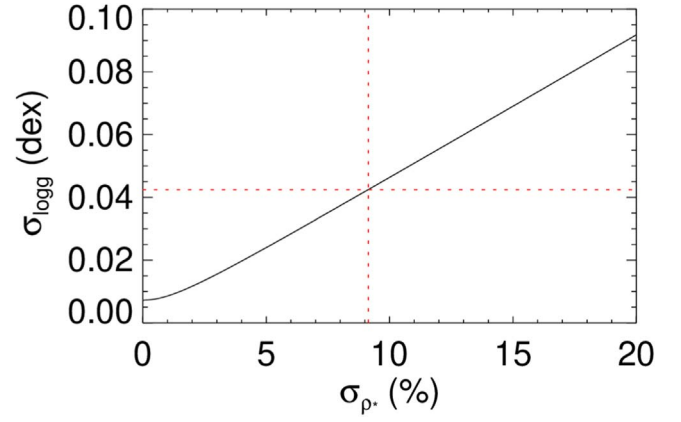

Figure 9. A plot of $\sigma_{\log g_*}$ as a function of σ_{ρ_*}, assuming $\sigma_{M_*} = 5\%$. The break-even point of $\log g_* = 0.042$ dex, where $\sigma_{M_*} = 5\%$ and from Tayar et al. (2022), is shown as a vertical red dashed line and corresponds to $\sigma_{\rho_*} \sim 9\%$.

we must ensure that our method does not introduce a new systematic error that is large compared to the systematic error in M_*. Therefore, we must ensure that the systematic errors on ρ_* from any source are below 2%, at which point the total model systematics are dominated by the systematic error already introduced by M_*.

The derivation of ρ_* from transits is straightforward and has been done in many places (e.g., Winn 2010). For context, we repeat it here. Starting with Kepler's law and the known planetary period, P,

$$P^2 = \frac{4\pi^2 a^3}{G(M_* + M_P)}, \quad (24)$$

we refactor in terms of ρ_* and solve,

$$\rho_* = \frac{3\pi}{GP^2}\left(\frac{a}{R_*}\right)^3 \frac{M_*}{M_* + M_P}. \quad (25)$$

If we wish, we can refactor Equation (25) in terms of R_P and ρ_P, which makes the negligible planetary term more obvious:

$$\rho_* = \frac{3\pi}{GP^2}\left(\frac{a}{R_*}\right)^3 - \left(\frac{R_P}{R_*}\right)^3 \rho_P. \quad (26)$$

Figure 3 shows that the 5% systematic error in M_* dominates as long as $\sigma_{\rho_*} \lesssim 2\%$, so here we enumerate potential sources of systematic error to let the reader understand when systematics in ρ_* might be the dominant consideration. When the sources of systematic error are well below that floor, no matter what statistical precision we achieve in ρ_*, we can trust the derived uncertainties in R_* and T_{eff}.

If the companion mass is less than 20 M_J for a solar-type star, ignoring the planetary mass entirely contributes less than 2% to the ρ_*, so we drop that term moving forward, and the fractional uncertainty in ρ_* becomes

$$\left(\frac{\sigma_{\rho_*}}{\rho_*}\right)^2 = \left(\frac{\sigma_P}{P}\right)^2 + \left(\frac{3\sigma_{a/R_*}}{a/R_*}\right)^2. \quad (27)$$

3.1. a/R_*

For the majority of systems, the most problematic component in computing ρ_* is a/R_*. The constraint comes down to

the signal-to-noise ratio and our ability to resolve the ingress and egress of the transit, and it is strongly degenerate with the planet's impact parameter. Not only is the measurement less straightforward, but its percent uncertainty is magnified by 3 when propagating to ρ_*, as we see in Equation (27).

3.1.1. Eccentricity

First, a/R_* is not the observable; the transit duration is. For nongrazing, circular orbits, the transit duration translates to a direct constraint on a/R_*, but for eccentric orbits, Winn (2010) showed that the observable is better approximated by

$$\frac{a}{R_*}\frac{\sqrt{1-e^2}}{1+e\sin\omega_*}. \tag{28}$$

This means that we must also know or assume the planetary eccentricity and argument of periastron independently from the light curve. Equation (79) and Figure 10 in Stevens et al. (2018) show that, for an eccentricity known to better than $\sim$1.5%—and more lax for smaller eccentricities—the uncertainty in e contributes negligibly to the uncertainty in ρ_*. We note that Stevens et al. (2018) assume that the covariance between eccentricity and ρ_* is negligible, which is true when the eccentricity is measured independently. This is not true when the eccentricity is derived from the light curve itself, but in that case the light curve's power to determine an independent ρ_* is limited.

Planets in very short periods can be assumed to be tidally circularized (Adams & Laughlin 2006). Given the small impact at low eccentricities, even if the planet is not strictly circularized, the error introduced to ρ_* is indeed negligible.

For other systems, we must rely on RVs, and we inherit the systematic errors of the spectrograph. The impact on the inferred eccentricity depends heavily on the spectrograph and the planet. In many cases, particularly for hot Jupiters most amenable to measuring ρ_*, the statistical error dominates the systematic error, but for systems where the RV semiamplitude is comparable to the instrumental precision, the systematic uncertainty may dominate.

Or, we can rely on the combination of the timing and duration of both the primary and secondary transit, inheriting the systematic errors of the photometric instrument and the clock. This typically yields extremely precise measurements of eccentricity, well below 1.5%.

In the future, we may be able to use Gaia DR4 to determine the eccentricity for a handful of (nearby, long-period) transiting systems, inheriting the systematic errors on its astrometry.

Ultimately, we need to be mindful of systematic error sources when the eccentricity uncertainty exceeds $\sim$1.5%—which is often and is likely to limit the number of stars where we can do such measurements. A campaign to measure precise eccentricities through secondary eclipse timing may dramatically broaden the number of stars where this technique is practical.

3.1.2. Grazing Transits

When the transit is grazing, significant degeneracies are introduced between the duration (i.e., a/R_*), inclination, and planetary radius. Because of that degeneracy, it is unlikely that grazing transits will provide a sufficient constraint on a/R_* ($\sigma_{\rho_*} \lesssim 10\%$) to improve the stellar parameters.
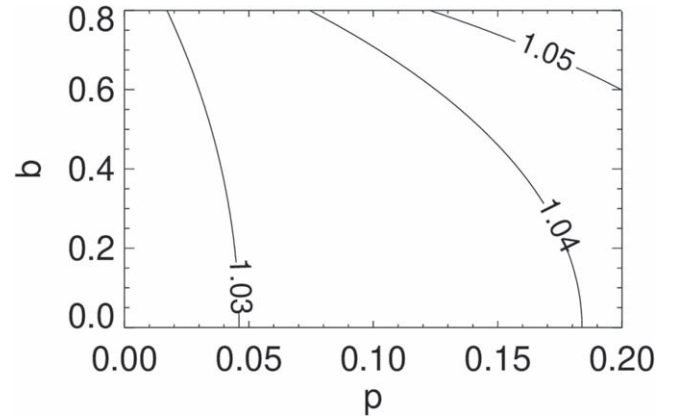

Figure 10. A contour plot showing the maximum allowed unaccounted blend in the transit light curve as a function of impact parameter b and planet-to-star radius ratio p such that its systematic impact ρ_* is below the 2% systematic impact from M_*. That is, the leftmost contour shows the family of planets whose systematics on the light-curve-determined ρ_* would be dominated by blends larger than 3% of the host star flux. Stated differently, as long as the unaccounted flux was less than 3%, the largest source of systematic error in the model would come from M_*.

3.1.3. Blending and Starspots

Blending from sources of light other than the star dilutes the transit light curve, biasing ρ_*, as discussed in detail by Kipping (2014). Because blending only makes the observed transit depth smaller than it is, it can only underestimate the light-curve-derived stellar density. Equation (9) in Kipping (2014) computes the bias on ρ_* as a function of the observed $p = R_P/R_*$, the observed impact parameter b, and the blend fraction $\mathcal{B}$, reproduced here:

$$\left(\frac{\rho_{*,\text{obs}}}{\rho_{*,\text{true}}}\right) = \mathcal{B}^{-3/4}\left(\frac{(1+\sqrt{\mathcal{B}}p)^2 - b^2}{(1+p)^2 - b^2}\right)^{3/2}. \tag{29}$$

We want to know the minimum contaminant, $\mathcal{B}$, that can cause a 2% error in the stellar density, or $\left(\frac{\rho_{*,\text{obs}}}{\rho_{*,\text{true}}}\right) = 0.98$. That error is technically unbounded as the numerator approaches zero, or when $b = 1 + p$. However, as we discussed in the previous section, grazing planets are already problematic and should not be used to infer the stellar density, so we will only consider nongrazing ($b < 1 - p$) planets.

Figure 10 shows the maximum allowed blending as a function of b and p such that the systematic error contribution from blending is less than the systematic error contribution from M_*. For a typical hot Jupiter ($p = 0.1, b = 0.5$), this means that the maximum allowed flux from an unseen blended companion is 3.5%, which is an important consideration.

Starspots have a similar impact to blends, though they may make the star dimmer or brighter than its mean. For spot modulations with a similar amplitude to that above, be mindful of its systematic impact on ρ_*. A more detailed discussion may be found in Kipping (2014).

3.1.4. Transit Timing Variations, Transit Duration Variations, and Long Integration Times

Transit timing variations (TTVs), transit duration variations (TDVs), and long integration times all smear out the observed transit and systematically bias the inferred stellar density. In general, when TTVs are detectable, they should be accounted

for, meaning that only TTVs that are undetectable will bias the inferred stellar density. Kipping (2014) quantifies this dependence as

$$\sigma_{\rho_*} \lesssim 7.5 \frac{G^{1/3} \rho_*^{1/3}}{pP^{1/3}} \frac{\sigma_\tau}{N^{1/4}}, \tag{30}$$

which shows that the impact of not accounting for a 1-minute TTV, in the worst case of a central crossing transit, is about 10% for a Jupiter-sized planet—nominally five times our floor. For small planets, the impact is worse. Confirmed TTVs for the hot Jupiters most amenable to the best ρ_* precision are rare, but this is an important caveat to consider. Kipping (2014) also shows that the systematic impact of TDVs on ρ_* is similar to the impact from TTVs, but less important in practice owing to their relative rarity. When undetectable TTVs are a concern, we could fit for them and would naturally propagate the timing uncertainty into the ρ_* from the light curve, though this would necessarily reduce the resultant precision of ρ_*.

In general, long integration times smear out the transit in a way that is similar to TTVs. Fortunately, the exposure times are well-known and that smearing is easily modeled (e.g., in EXOFASTv2, for each light curve, the user may specify the exposure times and how many model points to interpolate). However, failing to do so introduces important systematic errors similar to neglected TTVs with an amplitude of the exposure time. Price & Rogers (2014) discuss this impact in detail, but for TESS and Kepler, that is typically well in excess of our target 2% floor.

3.1.5. Limb Darkening

An a priori constraint on the limb darkening is often derived from stellar atmospheric models. Theoretical limb-darkening coefficients can differ dramatically from empirical measurements, especially for nonsolar ($T_{\rm eff} \lesssim 5000$ K or $T_{\rm eff} \gtrsim 7000$ K) stars (Patel & Espinoza 2022). In addition, the common choice of a quadratic limb-darkening law is not, in detail, correct. As both a/R_* and the limb darkening depend on the shape of the transit, errors in the limb darkening may bias the inferred values of a/R_*.

With sufficiently precise light curves, we can measure the limb darkening directly and remove the reliance on the stellar atmospheric models. Even in simulated cases where the theoretical limb darkening differs from the actual limb darkening by 0.1 in each quadratic term (nominally twice the assumed model uncertainty), its impact on the stellar parameters is negligible. Still, we recommend that when the light curve is sufficiently precise to directly measure the limb darkening, theoretical limb-darkening tables (e.g., Claret & Bloemen 2011) should not be used to further constrain them. When using EXOFASTv2 in particular, if the reported precision of the limb-darkening parameters is smaller than the 0.05 systematic error assumed in the tables, the tables should not be used.

In addition, the choice of the limb-darkening law can still bias the fit. EXOFASTv2 only implements the quadratic limb-darkening law, introducing a systematic error floor. However, Mandel & Agol (2002) showed that the error introduced here is typically below the noise floor, and thus negligible as it propagates to ρ_*.

3.1.6. Non-Keplerian Motion

The foundation of our derivation of ρ_* is Kepler's law, but the presence of additional bodies and tidal forces means that nothing follows Kepler's law to infinite precision. For a system with TTVs, a/R_* changes over time, but surely that has no impact on the stellar density. EXOFASTv2 assumes Keplerian orbits, but computational time is the only reason we hesitate to implement an N-body code to compute the planetary orbits. Given that the transit duration and stellar density are never explicitly defined in the transit model, it is likely that an accurate computation of any non-Keplerian motion would provide a similar constraint on the stellar density, but a detailed investigation of this is beyond the scope of this paper.

3.2. Period

The planetary period is directly measured from the frequency of transits, leveraged with long baselines between transits, often resulting in part-per-billion precision in the planetary period. However, it is worth noting that we universally introduce a systematic error in the observed period that is statistically significant in many systems today. Because stars are moving with respect to the solar system barycenter frame, there is a light-travel time effect that changes the observed frequency of transits by the systemic velocity, γ, divided by the speed of light, c:

$$\Delta P = \gamma/c. \tag{31}$$

But the reported planetary period is universally given in the solar system barycenter frame. Given a typical systemic velocity of $\sim$10 km s^{-1}, this $\sim$30 ppm effect amounts to about 30 s in a 10-day period, which is easily measurable today for the vast majority of transiting systems. Even EXOFASTv2, which does transform the observed times to the target frame before computing the model, ignores this effect because the RV is often measured from a reference spectrum taken at an earlier time, and so the absolute systemic velocity is often unknown. In addition, reporting the true period in the target's barycentric frame would lead to confusion in propagating the ephemerides that are practically important.

However, the impact of this error on ρ_* (or any observable we care about) is dwarfed by other errors. The 30 ppm effect is 5000 times lower than our threshold, so we safely ignore it.

4. Implementation

Despite the simplicity of the argument, in many cases a fundamentally new approach must be developed to take advantage of it. We can no longer simply interpolate an evolutionary grid to find the stellar parameters, as is commonly done. Nor can we simply separate the stellar and planetary model, as is also often done. The additional stellar density constraint overconstrains the evolutionary model grids, requiring optimization of competing constraints while simultaneously respecting the systematic error floors inherent in the evolutionary and atmospheric models. In addition, the constraints are often correlated in important ways, and those covariances must be known and applied with care if iterating between the stellar and planetary models to improve the precision of both. It is not enough to apply Gaussian, uncorrelated priors with each iteration.

As far as we are aware, EXOFASTv2 is unique in this regard—among private and public exoplanet modeling

codes. The link between the stellar density and the transit photometry has been at the heart of EXOFAST since its inception (Eastman et al. 2013), and the link between $T_{\rm eff}$, R_*, and L_* has been coded within EXOFASTv2 since SED fitting was added in 2017 January (Eastman et al. 2019). Despite only deeply understanding the mechanism now, EXOFASTv2 has long respected these relations and has been capable of using the transit-derived density to determine stellar parameters that are less dependent on the systematic floors of evolutionary models.

However, until Gaia DR2 in 2018 April, we could not always measure sufficiently precise luminosities, and up until 2020 October, we ignored systematic errors in the SED model, which resulted in many fits with underestimated uncertainties. In 2022 July, another update now allows users to specify their own systematic error floors on the stellar evolutionary models so that they may more accurately reflect those found by Tayar et al. (2022) rather than use the default ad hoc systematic error floors as a function of stellar mass described in Eastman et al. (2019) and summarized in Equation (32):

$$\sigma = 0.03 - 0.025 \log M_* + 0.045 (\log M_*)^2 . \tag{32}$$

We warn the user that the sample used by Tayar et al. (2022) consisted of near solar-type stars, and for such stars Tayar et al. (2022) showed that the default $\sim$3% errors EXOFASTv2 uses are likely slight underestimates of the systematic floors. However, for lower-mass stars, the systematic errors are likely much larger than the sample Tayar et al. (2022) explored, and our default ad hoc value of $\sim$10% is likely more appropriate. In addition, the detailed results from Tayar et al. (2022) were highly system dependent, and our blanket values of the systematic floor are simplified for the sake of presentation.

Finally, while the true nature of systematic errors is still poorly understood, we presume that all theoretical models share similar systematics, and so any combination of stellar theoretical models should not drive the uncertainties below the floors described in Tayar et al. (2022). When using multiple theoretical models (e.g., MIST and SED) with separate floors on the same parameters, it may be necessary to further inflate the individual systematic errors to achieve the desired total systematic floor in a star-only fit. Checking that the floors are as desired with a star-only fit is a good standard practice.

5. WASP-4b

While this analytic derivation is helpful for understanding where the information comes from and why, we assume that errors are Gaussian and uncorrelated, which is not strictly true. In this section, we model WASP-4b using EXOFASTv2 (Eastman et al. 2019) to confirm and validate our analytic formulae. A Markov Chain Monte Carlo code like EXOFASTv2 does not assume that the errors are Gaussian or uncorrelated, and so we can check that our analytic assumptions are reasonable by fitting a real-world system with a variety of constraints to check for such correlations and to see whether they re-create our uncorrelated expectations.

WASP-4b is a planet in a short period (1.34 days) that we can reasonably assume is tidally circularized, and so we know the eccentricity exactly, improving the precision in ρ_* (see Section 3.1.1 and Section 5.1). In addition, it has been observed in three TESS sectors at 2-minute cadence (which can be found in MAST: 10.17909/t9-nmc8-f686), with a very long baseline

between the TESS observations and the eight discovery light curves in 2007 (Wilson et al. 2008; Gillon et al. 2009; Winn et al. 2009). Many of those discovery light curves were observed in Sloan z' band, and the transit is nearly edge-on, which minimizes the covariance between density, impact parameter, and limb darkening. Finally, the transit is very deep (2.4%). All of these combine to enable us to measure the stellar density of WASP-4 to extreme precision.

A detailed exploration of what contributes to the statistical precision of ρ_* and an exhaustive search for the best candidate(s) is beyond the scope of this paper, but for the reasons above, WASP-4 is likely among the best-suited exoplanet hosts for measuring ρ_*. At any rate, for using ρ_* to measure R_* and $T_{\rm eff}$, there are diminishing returns beyond a ρ_* precision of $\sim$2% because the systematic floor in M_* begins to dominate.

Because of the way the evolutionary model is implemented with EXOFASTv2, we can only impose error floors in derived quantities like age, R_*, [Fe/H], and $T_{\rm eff}$, not the grid parameters M_*, $[{\rm Fe/H}]_0$, and the equal evolutionary phase (EEP; see Dotter 2016). Further, it was unclear to us how the systematic floors from the evolutionary models might combine with the systematic floors from the atmospheric models within EXO-FASTv2. We presume that both are limited by our understanding of the underlying stellar astrophysics, and so they should not combine as independent constraints. Instead, the combined MIST+SED models should still be limited by these same systematic floors: 2.4% in $F_{\rm bol}$, 4.2% in R_*, 5% in M_*, 2.0% in $T_{\rm eff}$, and 0.08 dex in [Fe/H]. However, this is complicated by the fact that we cannot tune these final floors directly, and the physical relation between these parameters often means that we cannot respect all floors exactly and simultaneously.

We began by doing a preliminary fit of only the WASP-4 host star including an SED fit of Gaia, 2MASS, and WISE broadband photometry; a MIST stellar evolutionary model (Paxton et al. 2011, 2013, 2015; Choi et al. 2016; Dotter 2016); priors on $[{\rm Fe/H}] = -0.03 \pm 0.09$ (Gillon et al. 2009); parallax $= 3.797 \pm 0.061$ mas (Gaia Collaboration et al. 2018); and an upper limit on the V-band extinction of 0.04278 mag based on galactic dust maps (Schlegel et al. 1998; Schlafly & Finkbeiner 2011). While a spectroscopic prior was available for $T_{\rm eff}$, we chose not to use it, as the $\sim$2% systematic uncertainty expected is much higher than the uncertainty we expect from our method described in Section 2.3. For reference, Wilson et al. (2008) found $T_{\rm eff} = 5500 \pm 150$ K using CORALIE, and Gillon et al. (2009) found $T_{\rm eff} = 5470 \pm 130$ K using IRFM, which is in good agreement (0.4σ) with our final recommended value of 5419^{+65}_{-63} K from the MIST + transit + SED fit.

We first fit a MIST+SED model with floors in the evolutionary model R_* of 4.2%, $T_{\rm eff}$ of 2.0%, and [Fe/H] of 0.08 dex, and SED model floors of 2.4% in $F_{\rm bol}$, 2.0% in $T_{\rm eff}$, and 0.08 dex in [Fe/H]. However, the combined constraint was lower than our model floors should be trusted. Hence, we inflated the R_* and $T_{\rm eff}$ systematic floors by $\sqrt{2}$ and refit. The model floors were still not exactly as desired because we cannot match them all at once owing to their influence on one another. They were close, but the best way to reconcile these competing constraints is unclear. In the MIST+SED column of Table 3, we see that our final constraints are close to our desired floors: 3.2% in $F_{\rm bol}$, 3.8% in R_*, 5.5% in M_*, 2.2% in $T_{\rm eff}$, and 0.084 dex in [Fe/H].

Table 2
Priors Imposed on All WASP-4b Fits

Parameter	Units	Prior
M_*	Mass ($M_\odot$)	$\mathcal{U}[0.694, 1.104]$
R_*	Radius ($R_\odot$)	$\mathcal{U}[0.83, 0.97]$
$T_{\rm eff}$	Effective temperature (K)	$\mathcal{U}[5120, 5735]$
[Fe/H]	Metallicity (dex)	$\mathcal{G}[-0.03, 0.09]$
A_V	V-band extinction (mag)	$\mathcal{U}[0, 0.04278]$
ϖ	Parallax (mas)	$\mathcal{G}[3.7965, 0.0608]$
e	Eccentricity	0 (fixed)
ω_*	Argument of periastron (deg)	90 (fixed)

It would be best to do a thorough investigation that explores systematic differences between models similar to Tayar et al. (2022) or Duck et al. (2022) for each modeled system and set these floors accordingly, but this is a major effort and likely impractical for all systems.

Next, we performed eight different fits of the WASP-4 system with all combinations of with and without the SED model, the MIST model, and the transit model, including no model constraints, labeled "None," showing just our prior constraints. Each fit was constrained with the same wide, uniform priors summarized in Table 2, equal to five times the 68% confidence interval of the preliminary MIST+SED fit described above. These are wide enough not to appreciably influence fits that were reasonably well constrained, but narrow enough to allow the fits to mix in the absence of any external constraints, see the impact of our chosen stepping parameters, and ensure that the only things that changed between fits were the models used to constrain them. In the case where we do not fit the SED, MIST, or transit model, the posteriors are equal to these priors. All fits had the same systematic error floors imposed where applicable.

For all fits including transits, we included the 14 discovery RVs from CORALIE (Wilson et al. 2008); eight early, complete light curves (Wilson et al. 2008; Gillon et al. 2009; Winn et al. 2009); and the flattened, 2-minute SPOC TESS light curves from sectors 2, 28, and 29. The transit data spanned 13 yr and 3545 epochs. We disabled the limb-darkening table look-up from Claret & Bloemen (2011) to avoid introducing any systematic errors (Patel & Espinoza 2022) and fit the quadratic limb-darkening parameters in each band directly. We assumed that the orbit was circular.

In Figure 11, we show the corner plot of the stellar parameters for the three most relevant fits—the MIST+SED, transit-only, and MIST+transit+SED. As expected, we see that ρ_* uncertainty is dramatically reduced with the transit, and due to its covariance with R_* and $T_{\rm eff}$, their uncertainties are also significantly reduced. We also see that the combination of MIST, SED, and the transit is somewhat more complex than our mathematical assumption that the errors are Gaussian and uncorrelated. The slight covariance between M_* and R_* in the MIST+SED fit means that when we add the transit, we also slightly improve the constraint on M_* ($\sim$10%).

As can be seen in the last column of Table 3, using MIST, the SED, and the transit model allows us to measure the stellar density to 1.2%. Despite the models using the floors above, we are able to infer M_* to 4.8%, R_* to 1.6%, and $T_{\rm eff}$ to 1.1%, in line with our analytic expectations given such a precise ρ_*. We

note that here we do not achieve the 0.9% precision expected from Figure 4 because the uncertainty in the distance is not negligible and we do not reach the floor in $F_{\rm bol}$, likely because WASP-4 is a relatively faint planet host ($V = 12.5$). With the $\sigma_d = 1.5\%$, $\sigma_{F_{\rm bol}} = 2.9\%$, and $\sigma_{R_*} = 1.6\%$ we achieve, Equation (14) predicts a $\sigma_{T_{\rm eff}} = 1.3\%$, in good agreement with our measurement of 1.1%.

The improvement of the planetary parameters, summarized in Tables 4 and 5, is also significant. However, we must be careful because EXOFASTv2 cannot sever the connection between the transit model and the stellar density. Table 4 shows all the fits that include the transit and so are direct outputs from EXOFASTv2. Table 5 shows the rederived planetary parameters using the star-only values in the corresponding column of Table 3 combined with the transit-observables taken from the transit-only fit—thus re-creating methods that model the star and planet separately.

These transit-observables span all columns in Table 5 and agree with each other to at least 0.1σ in all fits using a transit in Table 4. Thus, comparing the MIST+Transit+SED column in Table 4 with the MIST+SED column in Table 5 shows the improvement in the planetary parameters that is achievable when we account for realistic systematic floors in the stellar models, we have a strong constraint on stellar density, and we model the star and planet simultaneously.

Most importantly, the precision in the planet's radius, density, surface gravity, semimajor axis, and incident flux improves by about a factor of two. The improvement in $T_{\rm eq}$ is equally significant, but it is likely that our statistical uncertainties are dominated by the assumptions that there is no albedo and perfect redistribution. However, the incident flux is improved by a similar factor and is an important, fundamental component of the detailed atmospheric modeling necessary to truly understand the equilibrium temperature and habitability more broadly.

5.1. Tidal Circularization

In general, the eccentricity of hot Jupiters is likely not exactly zero, but ignoring the difference between its actual eccentricity and 0 introduces a negligible error in ρ_* compared to our 2% goal (beyond which the measurement is dominated by M_* systematics).

One could reasonably argue that we should use the observational constraints on eccentricity such that the presumption of circularity does not bias our measurement of ρ_*. However, for WASP-4 and many hot Jupiters, the observational constraints on the eccentricity are poor and do not account for the strong theoretical expectation we have for tidal circularization. Therefore, the observational limits represent a very conservative upper limit on the allowed eccentricity, which translates to an unnecessarily conservative uncertainty on ρ_*.

Wang & Ford (2011) explored the eccentricity distribution of such short-period planets, but their sample only had a single planet with a period comparable to WASP-4 (HD41004B), and its eccentricity is consistent with zero ($e = 0.058^{+0.051}_{-0.058}$). They had no planets with a tidal circularization timescale comparable to the 2.8 Myr we compute for WASP-4b, but all the planets in their sample with a tidal circularization timescale of less than 1 Gyr had an eccentricity consistent with zero.
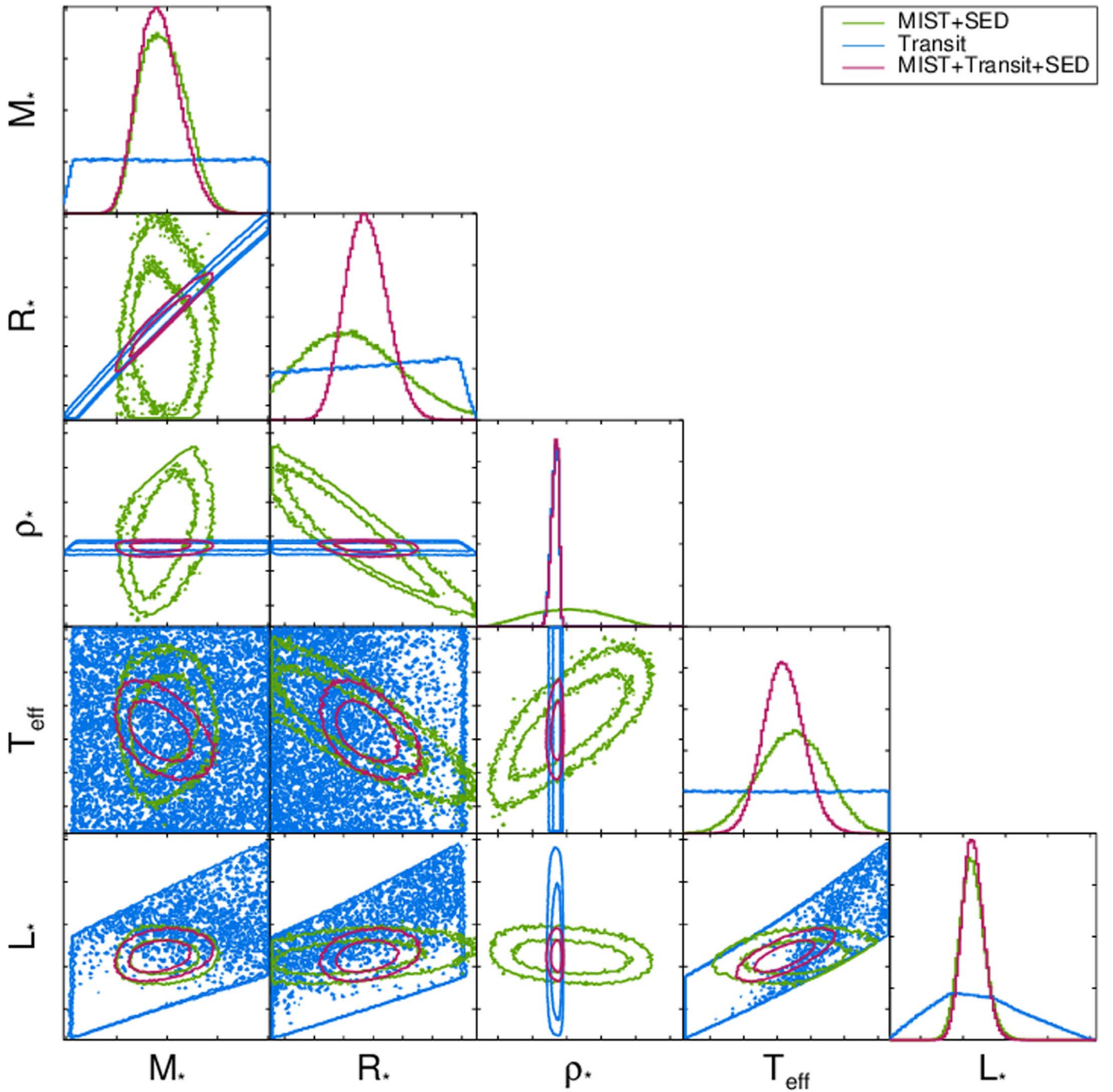
Figure 11. A corner plot of the WASP-4 stellar parameters. The contours show the 68% and 95% confidence intervals for the MIST+SED fit (green), the transit-only fit (blue), and the MIST+transit+SED fit (magenta). From this, we can see just how the addition of the transit constrains the stellar density and significantly improves the precision of R_* and T_{eff}—to well beyond the systematic floors imposed on the SED and MIST evolutionary models. The areas under each curve in the histograms are proportional to likelihood and are normalized to have the same area between each of the fits for a given parameter. For ρ_* in particular, we can see the huge impact the transit has on shifting the probability to a narrow, high peak.

Ultimately, our goal is to compute the most precise and accurate stellar parameters, and to do that, we believe that the theoretical expectation of tidal circularization (at least in the case of WASP-4b) is more reliable than our theoretical understanding for stellar evolution. However, we should be clear that it is still generally useful to fit for eccentricity so that we can test the theoretical expectations of tidal circularization, rather than assume it as we do here.

6. Discussion

Among the set of 1145 default (`DEFAULT_FLAG=1`) transiting planets (`TRAN_FLAG=1`) in the exoplanet archive where the stellar density and its uncertainty are populated, 56 have host stars with a fractional ρ_* uncertainty less than 2%. It grows to 426 systems if we use a threshold of 9% (where we can beat the systematic floor in the SED/MIST-derived $\log g_*$), 503 systems if we use a threshold of 10.3% (where we can beat

Table 3
Median Values and 68% Confidence Interval for the WASP-4 Host Star with All Eight Combinations of Using or Not Using the SED, MIST, or Transit Constraint

Parameter	Units	None	MIST	SED	MIST+SED	Transit	Transit+SED	MIST+Transit	MIST+Transit+SED
M_*	Mass ($M_\odot$)	$0.88^{+0.15}_{-0.13}$	$0.879^{+0.056}_{-0.048}$	$0.88^{+0.15}_{-0.13}$	$0.895^{+0.052}_{-0.046}$	$0.91^{+0.13}_{-0.14}$	$0.88^{+0.13}_{-0.11}$	$0.890^{+0.070}_{-0.057}$	$0.886^{+0.046}_{-0.040}$
R_*	Radius ($R_\odot$)	$0.900^{+0.046}_{-0.047}$	$0.890^{+0.049}_{-0.041}$	$0.890^{+0.044}_{-0.038}$	$0.886^{+0.035}_{-0.032}$	$0.903^{+0.043}_{-0.048}$	$0.893^{+0.041}_{-0.038}$	$0.898^{+0.023}_{-0.020}$	$0.896^{+0.015}_{-0.014}$
L_*	Luminosity ($L_\odot$)	$0.631^{+0.12}_{-0.097}$	$0.63^{+0.12}_{-0.10}$	$0.624^{+0.029}_{-0.028}$	$0.624^{+0.030}_{-0.027}$	$0.631^{+0.12}_{-0.097}$	$0.624^{+0.028}_{-0.026}$	0.65 ± 0.11	$0.625^{+0.028}_{-0.026}$
ρ_*	Density (cgs)	$1.70^{+0.38}_{-0.31}$	$1.76^{+0.24}_{-0.23}$	$1.74^{+0.37}_{-0.30}$	$1.82^{+0.24}_{-0.22}$	$1.737^{+0.019}_{-0.025}$	$1.737^{+0.019}_{-0.025}$	$1.738^{+0.018}_{-0.019}$	$1.738^{+0.018}_{-0.024}$
$\log g$	Surface gravity (cgs)	4.473 ± 0.074	$4.483^{+0.039}_{-0.042}$	$4.480^{+0.074}_{-0.073}$	$4.495^{+0.041}_{-0.042}$	$4.484^{+0.020}_{-0.024}$	$4.479^{+0.020}_{-0.019}$	$4.481^{+0.011}_{-0.010}$	$4.4809^{+0.0080}_{-0.0078}$
$T_{\rm eff}$	Effective temp (K)	5430^{+210}_{-200}	5440^{+180}_{-190}	5440 ± 120	5450 ± 100	5420 ± 210	5430 ± 120	5470^{+180}_{-200}	5419^{+65}_{-63}
[Fe/H]	Metallicity (dex)	-0.031 ± 0.087	-0.025 ± 0.089	$0.011^{+0.085}_{-0.083}$	$0.012^{+0.082}_{-0.080}$	$-0.031^{+0.091}_{-0.090}$	$0.013^{+0.082}_{-0.079}$	$-0.021^{+0.089}_{-0.088}$	$0.015^{+0.082}_{-0.078}$
$R_{*,\rm SED}$	Radius[1] ($R_\odot$)	$\cdots$	$\cdots$	$0.882^{+0.017}_{-0.016}$	$0.882^{+0.017}_{-0.016}$	$\cdots$	0.882 ± 0.016	$\cdots$	$0.883^{+0.016}_{-0.015}$
$F_{\rm Bol}$	Bol flux $\times 10^{10}$ (cgs)	$\cdots$	$\cdots$	$2.867^{+0.098}_{-0.088}$	$2.870^{+0.095}_{-0.088}$	$\cdots$	$2.866^{+0.092}_{-0.082}$	$\cdots$	$2.867^{+0.088}_{-0.082}$
$T_{\rm eff,SED}$	Effective temp[a] (K)	$\cdots$	$\cdots$	5461^{+34}_{-31}	5462^{+33}_{-30}	$\cdots$	5461^{+31}_{-29}	$\cdots$	5460^{+30}_{-29}
[Fe/H]$_{\rm SED}$	Metallicity (dex)	$\cdots$	$\cdots$	$0.038^{+0.11}_{-0.092}$	$0.042^{+0.11}_{-0.096}$	$\cdots$	$0.043^{+0.10}_{-0.089}$	$\cdots$	$0.043^{+0.11}_{-0.087}$
A_V	V-band ext (mag)	$\cdots$	$\cdots$	$0.022^{+0.014}_{-0.015}$	$0.023^{+0.014}_{-0.015}$	$\cdots$	$0.023^{+0.014}_{-0.015}$	$\cdots$	$0.023^{+0.014}_{-0.015}$
$\sigma_{\rm SED}$	SED error scaling	$\cdots$	$\cdots$	$1.02^{+0.41}_{-0.24}$	$1.01^{+0.40}_{-0.24}$	$\cdots$	$0.98^{+0.34}_{-0.22}$	$\cdots$	$0.97^{+0.33}_{-0.21}$
ϖ	Parallax (mas)	$\cdots$	$\cdots$	3.791 ± 0.061	3.791 ± 0.061	$\cdots$	$3.791^{+0.059}_{-0.060}$	$\cdots$	$3.789^{+0.059}_{-0.060}$
d	Distance (pc)	$\cdots$	$\cdots$	$263.8^{+4.3}_{-4.2}$	$263.8^{+4.3}_{-4.2}$	$\cdots$	$263.8^{+4.2}_{-4.1}$	$\cdots$	$264.0^{+4.2}_{-4.1}$
[Fe/H]$_0$	Initial metallicity[b]	$\cdots$	-0.00 ± 0.11	$\cdots$	0.03 ± 0.10	$\cdots$	$\cdots$	0.00 ± 0.11	$0.033^{+0.10}_{-0.099}$
Age	Age (Gyr)	$\cdots$	$7.0^{+4.4}_{-3.7}$	$\cdots$	$6.2^{+4.7}_{-3.9}$	$\cdots$	$\cdots$	$6.6^{+4.4}_{-4.0}$	$7.3^{+3.7}_{-3.8}$
EEP	Equal evol phase[c]	$\cdots$	351^{+37}_{-18}	$\cdots$	350^{+37}_{-27}	$\cdots$	$\cdots$	351^{+33}_{-23}	356^{+32}_{-22}

Notes. See Table 3 in Eastman et al. (2019) for a detailed description of all parameters.
[a] This value ignores the systematic error and is for reference only.
[b] The metallicity of the star at birth.
[c] Corresponds to static points in a star's evolutionary history. See Section 2 in Dotter (2016).

Table 4
Median Values and 68% Confidence Interval for the WASP-4 Host Star

Parameter	Units	Transit	Transit+SED	MIST+Transit	MIST+Transit+SED
P	Period (days)	$1.338231512 \pm 0.000000019$	$1.338231512 \pm 0.000000019$	$1.338231512 \pm 0.000000019$	$1.338231513 \pm 0.000000019$
R_P	Radius (R_J)	$1.348^{+0.064}_{-0.071}$	$1.335^{+0.062}_{-0.058}$	$1.341^{+0.035}_{-0.030}$	$1.339^{+0.023}_{-0.021}$
M_P	Mass (M_J)	1.22 ± 0.13	$1.20^{+0.13}_{-0.11}$	$1.210^{+0.086}_{-0.081}$	$1.207^{+0.073}_{-0.071}$
T_C	Time of conjunction[a] (BJD$_{TDB}$)	$2454697.797524 \pm 0.000024$	$2454697.797525 \pm 0.000024$	$2454697.797524^{+0.000024}_{-0.000023}$	$2454697.797524 \pm 0.000023$
T_T	Time of min proj sep[b] (BJD$_{TDB}$)	$2454697.797524 \pm 0.000024$	$2454697.797525 \pm 0.000024$	$2454697.797524^{+0.000024}_{-0.000023}$	$2454697.797524 \pm 0.000023$
T_0	Optimal conj time[c] (BJD$_{TDB}$)	$2455337.472187 \pm 0.000022$	$2455348.178040 \pm 0.000022$	$2455336.133956 \pm 0.000022$	$2455329.442798 \pm 0.000022$
a	Semimajor axis (au)	$0.0230^{+0.0011}_{-0.0012}$	$0.02277^{+0.0010}_{-0.00099}$	$0.02287^{+0.00060}_{-0.00052}$	$0.02284^{+0.00040}_{-0.00037}$
i	Inclination (deg)	$88.87^{+0.67}_{-0.51}$	$88.87^{+0.67}_{-0.51}$	$88.89^{+0.66}_{-0.52}$	$88.89^{+0.65}_{-0.51}$
T_{eq}	Equilibrium temperature[d] (K)	1638^{+64}_{-63}	1639^{+35}_{-36}	1651^{+54}_{-61}	1637^{+20}_{-19}
τ_{circ}	Tidal circ timescale (Gyr)	$0.00277^{+0.00021}_{-0.00020}$	0.00279 ± 0.00021	0.00278 ± 0.00019	0.00279 ± 0.00018
K	RV semiamplitude (m s^{-1})	240 ± 12	240 ± 12	240 ± 12	240 ± 12
R_P/R_*	Radius of planet in stellar radii	$0.15348^{+0.00047}_{-0.00039}$	$0.15349^{+0.00047}_{-0.00040}$	$0.15348^{+0.00047}_{-0.00039}$	$0.15348^{+0.00046}_{-0.00039}$
a/R_*	Semimajor axis in stellar radii	$5.481^{+0.020}_{-0.026}$	$5.481^{+0.020}_{-0.026}$	$5.482^{+0.019}_{-0.026}$	$5.482^{+0.019}_{-0.026}$
δ	$(R_P/R_*)^2$	$0.02356^{+0.00014}_{-0.00012}$	$0.02356^{+0.00014}_{-0.00012}$	$0.02355^{+0.00015}_{-0.00012}$	$0.02355^{+0.00014}_{-0.00012}$
δ_R	Transit depth in R (fraction)	$0.03042^{+0.00086}_{-0.00081}$	$0.03044^{+0.00086}_{-0.00082}$	$0.03043^{+0.00086}_{-0.00081}$	$0.03043^{+0.00086}_{-0.00082}$
$\delta_{z'}$	Transit depth in z' (fraction)	$0.02781^{+0.00049}_{-0.00046}$	$0.02782^{+0.00049}_{-0.00047}$	$0.02782^{+0.00050}_{-0.00047}$	$0.02782^{+0.00049}_{-0.00046}$
δ_{TESS}	Transit depth in TESS (fraction)	$0.02867^{+0.00076}_{-0.00072}$	$0.02869^{+0.00075}_{-0.00071}$	$0.02869^{+0.00075}_{-0.00072}$	$0.02868^{+0.00076}_{-0.00071}$
τ	Ingress/egress transit duration (days)	$0.01220^{+0.00017}_{-0.00013}$	$0.01220^{+0.00017}_{-0.00013}$	$0.01220^{+0.00018}_{-0.00013}$	$0.01220^{+0.00017}_{-0.00012}$
T_{14}	Total transit duration (days)	0.08992 ± 0.00014	0.08992 ± 0.00014	0.08992 ± 0.00014	0.08992 ± 0.00014
T_{FWHM}	FWHM transit duration (days)	$0.07770^{+0.00017}_{-0.00018}$	$0.07770^{+0.00017}_{-0.00018}$	$0.07770^{+0.00017}_{-0.00018}$	$0.07770^{+0.00017}_{-0.00018}$
b	Transit impact parameter	$0.108^{+0.048}_{-0.064}$	$0.109^{+0.048}_{-0.064}$	$0.106^{+0.049}_{-0.063}$	$0.106^{+0.048}_{-0.062}$
ρ_P	Density (cgs)	$0.620^{+0.045}_{-0.042}$	$0.624^{+0.042}_{-0.041}$	0.621 ± 0.036	0.623 ± 0.034
$\log g_P$	Surface gravity (cgs)	$3.222^{+0.022}_{-0.023}$	$3.222^{+0.021}_{-0.023}$	$3.222^{+0.021}_{-0.023}$	$3.222^{+0.021}_{-0.023}$
$\langle F \rangle$	Incident flux (10^9 erg s^{-1} cm^{-2})	$1.64^{+0.27}_{-0.24}$	$1.64^{+0.15}_{-0.14}$	$1.69^{+0.23}_{-0.24}$	$1.629^{+0.081}_{-0.075}$
T_S	Time of eclipse (BJD$_{TDB}$)	$2454698.466639 \pm 0.000024$	$2454698.466641 \pm 0.000024$	$2454698.466640^{+0.000024}_{-0.000023}$	$2454698.466640 \pm 0.000023$
$M_P \sin i$	Minimum mass (M_J)	1.22 ± 0.13	$1.20^{+0.13}_{-0.11}$	$1.210^{+0.086}_{-0.081}$	$1.206^{+0.073}_{-0.071}$
u_1	R linear limb-darkening coeff	0.460 ± 0.041	$0.461^{+0.041}_{-0.042}$	0.460 ± 0.041	$0.460^{+0.041}_{-0.042}$
u_2	R quadratic limb-darkening coeff	$0.152^{+0.075}_{-0.076}$	0.151 ± 0.076	$0.151^{+0.075}_{-0.076}$	$0.152^{+0.076}_{-0.075}$
u_1	z' linear limb-darkening coeff	$0.312^{+0.025}_{-0.024}$	0.313 ± 0.025	0.313 ± 0.025	$0.313^{+0.025}_{-0.024}$
u_2	z' quadratic limb-darkening coeff	$0.219^{+0.055}_{-0.057}$	$0.218^{+0.056}_{-0.057}$	$0.218^{+0.056}_{-0.058}$	$0.219^{+0.055}_{-0.057}$
u_1	TESS linear limb-darkening coeff	$0.364^{+0.041}_{-0.040}$	0.365 ± 0.040	0.365 ± 0.040	0.365 ± 0.040
u_2	TESS quadratic limb-darkening coeff	$0.141^{+0.075}_{-0.076}$	$0.139^{+0.074}_{-0.075}$	$0.139^{+0.074}_{-0.075}$	$0.140^{+0.074}_{-0.076}$

Notes. See Table 3 in Eastman et al. (2019) for a detailed description of all parameters.
[a] Time of conjunction is commonly reported as the "transit time."
[b] Time of minimum projected separation is a more correct "transit time."
[c] Optimal time of conjunction minimizes the covariance between T_C and period.
[d] Assumes no albedo and perfect redistribution.

Table 5
Median Values and 68% Confidence Interval for WASP-4b Planet Fits, Separating the Transit and Stellar Models

Parameter	Units	None	MIST	SED	MIST+SED
P	Period (days)		$1.338231512 \pm 0.000000019$		
R_P	Radius (R_J)	$1.345^{+0.069}_{-0.070}$	$1.330^{+0.073}_{-0.061}$	$1.330^{+0.066}_{-0.057}$	$1.323^{+0.053}_{-0.047}$
M_P	Mass (M_J)	$1.19^{+0.14}_{-0.12}$	$1.199^{+0.078}_{-0.074}$	$1.19^{+0.14}_{-0.12}$	$1.213^{+0.078}_{-0.074}$
T_C	Time of conjunction[a] ($\mathrm{BJD_{TDB}}$)		$2454697.797524 \pm 0.000024$		
T_T	Time of min proj sep[b] ($\mathrm{BJD_{TDB}}$)		$2454697.797524 \pm 0.000024$		
T_0	Optimal conj time[c] ($\mathrm{BJD_{TDB}}$)		$2455337.472187 \pm 0.000022$		
a	Semimajor axis (au)	0.0229 ± 0.0012	$0.0227^{+0.0012}_{-0.0010}$	$0.02268^{+0.0011}_{-0.00097}$	$0.02257^{+0.00090}_{-0.00081}$
i	Inclination (deg)		$88.87^{+0.67}_{-0.51}$		
$T_{\rm eq}$	Equilibrium temperature[d] (K)	1639 ± 62	1643^{+55}_{-57}	1642^{+36}_{-38}	1646 ± 31
$\tau_{\rm circ}$	Tidal circ timescale (Gyr)	$0.00281^{+0.00046}_{-0.00039}$	$0.00277^{+0.00027}_{-0.00025}$	$0.00278^{+0.00045}_{-0.00039}$	$0.00271^{+0.00027}_{-0.00025}$
K	RV semiamplitude (m s^{-1})		240 ± 12		
R_P/R_*	Radius of planet in stellar radii		$0.15348^{+0.00047}_{-0.00039}$		
a/R_*	Semimajor axis in stellar radii		$5.481^{+0.020}_{-0.026}$		
δ	$(R_P/R_*)^2$		$0.02356^{+0.00014}_{-0.00012}$		
δ_R	Transit depth in R (fraction)		$0.03042^{+0.00086}_{-0.00081}$		
$\delta_{z'}$	Transit depth in z' (fraction)		$0.02781^{+0.00049}_{-0.00046}$		
$\delta_{\rm TESS}$	Transit depth in TESS (fraction)		$0.02867^{+0.00076}_{-0.00072}$		
τ	Ingress/egress transit duration (days)		$0.01220^{+0.00017}_{-0.00013}$		
T_{14}	Total transit duration (days)		0.08992 ± 0.00014		
$T_{\rm FWHM}$	FWHM transit duration (days)		$0.07770^{+0.00017}_{-0.00018}$		
b	Transit impact parameter		$0.108^{+0.048}_{-0.064}$		
ρ_P	Density (cgs)	$0.609^{+0.12}_{-0.099}$	$0.630^{+0.094}_{-0.088}$	$0.627^{+0.11}_{-0.097}$	$0.648^{+0.087}_{-0.082}$
$\log g_P$	Surface gravity (cgs)	$3.214^{+0.061}_{-0.062}$	$3.224^{+0.044}_{-0.046}$	3.222 ± 0.059	$3.234^{+0.042}_{-0.044}$
$\langle F \rangle$	Incident flux (10^9 erg s^{-1} cm^{-2})	$1.64^{+0.26}_{-0.23}$	$1.66^{+0.23}_{-0.22}$	1.65 ± 0.15	$1.67^{+0.13}_{-0.12}$
T_S	Time of eclipse ($\mathrm{BJD_{TDB}}$)		$2454698.466639 \pm 0.000024$		
$M_P \sin i$	Minimum mass (M_J)	$1.19^{+0.14}_{-0.12}$	$1.198^{+0.078}_{-0.074}$	$1.19^{+0.14}_{-0.12}$	$1.213^{+0.078}_{-0.074}$
u_1	R linear limb-darkening coeff		0.460 ± 0.041		
u_2	R quadratic limb-darkening coeff		$0.152^{+0.075}_{-0.076}$		
u_1	z' linear limb-darkening coeff		$0.312^{+0.025}_{-0.024}$		
u_2	z' quadratic limb-darkening coeff		$0.219^{+0.055}_{-0.057}$		
u_1	TESS linear limb-darkening coeff		$0.364^{+0.041}_{-0.040}$		
u_2	TESS quadratic limb-darkening coeff		$0.141^{+0.075}_{-0.076}$		

Notes. Values that span all columns are taken from the transit-only fit. See Table 3 in Eastman et al. (2019) for a detailed description of all parameters.
[a] Time of conjunction is commonly reported as the "transit time."
[b] Time of minimum projected separation is a more correct "transit time."
[c] Optimal time of conjunction minimizes the covariance between T_C and period.
[d] Assumes no albedo and perfect redistribution.

the systematic floor in the SED/MIST-derived R_*), and 556 systems if we use a threshold of 11.5% (where we can beat the systematic floor in the spectroscopic $T_{\rm eff}$).

These are likely a significant undercount of the number of systems suitable to such precision given the heterogeneity of the sample, the relative rarity of simultaneous modeling of the star and planet, and the fact that only 30% of the default set of transiting planets even have stellar densities populated. It is possible that some of these densities are optimistically derived from evolutionary models while ignoring systematic errors rather than a transit light curve. However, only 6% of nontransiting planets have quoted stellar densities compared to 30% of transiting planets, implying that the transit was used for most when available.

Regardless, this technique could likely be applied to a significant fraction of transiting planet hosts to improve the stellar and planetary parameters. Even nontransiting planet hosts are likely to see improved $\log g_*$ precision, as described in

Section 2.5, which can be used to improve spectroscopic measurements of $T_{\rm eff}$ and [Fe/H]. While a precision similar to what we achieve here is commonly reported in the literature, few have accounted for the systematic uncertainties in the stellar parameters shown by Tayar et al. (2022), and so they may be too optimistic.

The results shown here emphasize just how important it is to model the star along with the planet to improve the precision of both. It is possible that a large sample of well-measured transit light curves may even help inform stellar models. This method is competitive with gold standard measurements like asteroseismology or eclipsing binary stars but broadens the pool of applicable stars dramatically. This, in turn, could give us a precise probe into stellar parameters that enable us to test and refine the evolutionary models. Because our derived parameters are still limited by systematics in the stellar models, further improvement in stellar models would yield additional refinement with currently known stellar densities. It may even be

fruitful to explore how best to take advantage of the precise stellar density and bolometric flux constraints when constructing the evolutionary models themselves, as these are directly and precisely measured for a much larger sample of stars than are typically used to anchor stellar models.

ORCID iDs

Jason D. Eastman ⓘ https://orcid.org/0000-0003-3773-5142
Hannah Diamond-Lowe ⓘ https://orcid.org/0000-0001-8274-6639
Jamie Tayar ⓘ https://orcid.org/0000-0002-4818-7885

References

Adams, F. C., & Laughlin, G. 2006, ApJ, 649, 1004
Bastien, F. A., Stassun, K. G., Basri, G., & Pepper, J. 2013, Natur, 500, 427
Bastien, F. A., Stassun, K. G., Basri, G., & Pepper, J. 2016, ApJ, 818, 43
Beatty, T. G., Stevens, D. J., Collins, K. A., et al. 2017, AJ, 154, 25
Choi, J., Dotter, A., Conroy, C., et al. 2016, ApJ, 823, 102
Claret, A., & Bloemen, S. 2011, A&A, 529, A75
Dotter, A. 2016, ApJS, 222, 8
Duck, A., Gaudi, B. S., Eastman, J. D., & Rodriguez, J. E. 2022, arXiv:2209.09266
Eastman, J., Gaudi, B. S., & Agol, E. 2013, PASP, 125, 83
Eastman, J. D., Rodriguez, J. E., Agol, E., et al. 2019, arXiv:1907.09480
Gaia Collaboration, Brown, A. G. A., Vallenari, A., et al. 2016, A&A, 595, A2
Gaia Collaboration, Brown, A. G. A., Vallenari, A., et al. 2018, A&A, 616, A1
Gillon, M., Smalley, B., Hebb, L., et al. 2009, A&A, 496, 259
Kipping, D. M. 2014, MNRAS, 440, 2164
Lindegren, L., Bastian, U., Biermann, M., et al. 2021, A&A, 649, A4
Lindegren, L., Hernández, J., Bombrun, A., et al. 2018, A&A, 616, A2
Mandel, K., & Agol, E. 2002, ApJL, 580, L171
Patel, J. A., & Espinoza, N. 2022, AJ, 163, 228
Paxton, B., Bildsten, L., Dotter, A., et al. 2011, ApJS, 192, 3
Paxton, B., Cantiello, M., Arras, P., et al. 2013, ApJS, 208, 4
Paxton, B., Marchant, P., Schwab, J., et al. 2015, ApJS, 220, 15
Price, E. M., & Rogers, L. A. 2014, ApJ, 794, 92
Sandford, E., & Kipping, D. 2017, AJ, 154, 228
Schlafly, E. F., & Finkbeiner, D. P. 2011, ApJ, 737, 103
Schlegel, D. J., Finkbeiner, D. P., & Davis, M. 1998, ApJ, 500, 525
Seager, S., & Mallén-Ornelas, G. 2003, ApJ, 585, 1038
Skrutskie, M. F., Cutri, R. M., Stiening, R., et al. 2006, AJ, 131, 1163
Stassun, K. G., & Torres, G. 2018, ApJ, 862, 61
Stevens, D. J., Gaudi, B. S., & Stassun, K. G. 2018, ApJ, 862, 53
Tayar, J., Claytor, Z. R., Huber, D., & van Saders, J. 2022, ApJ, 927, 31
Torres, G., Fischer, D. A., Sozzetti, A., et al. 2012, ApJ, 757, 161
Wang, J., & Ford, E. B. 2011, MNRAS, 418, 1822
Wilson, D. M., Gillon, M., Hellier, C., et al. 2008, ApJL, 675, L113
Winn, J. N. 2010, arXiv:1001.2010
Winn, J. N., Holman, M. J., Carter, J. A., et al. 2009, AJ, 137, 3826
Winn, J. N., Holman, M. J., Torres, G., et al. 2008, ApJ, 683, 1076
Wright, E. L., Eisenhardt, P. R. M., Mainzer, A. K., et al. 2010, AJ, 140, 1868
Zinn, J. C., Pinsonneault, M. H., Huber, D., & Stello, D. 2019, ApJ, 878, 136